

Observations of the 2011 Shinmoedake eruptions

Detailed seismological and geodetic observations were conducted from Apr. 2010 onward. After the sub-Plinian eruptions, monitoring networks were expanded and more abundant stations were operated within the network (e.g., Nakada et al., 2013). No clear precursors were recorded at the observation stations prior to the major eruptions; this suggests that the erupted magma was stored in a shallow part of an existing conduit before the beginning of the eruption (Ueda et al., 2013). On the basis of satellite synthetic aperture radar images, the magma discharge rate was estimated to be 450–741 m³s⁻¹ in dense rock equivalent (DRE) in the sub-Plinian stage and 70.0–87.4 m³s⁻¹ in the lava effusion and vulcanian explosion stages (Kozono et al., 2013). The SO₂ in the volcanic plumes was analyzed by differential optical absorption spectroscopy from Jan. 27 to Apr. 6. High SO₂ flux was observed immediately after the sub-Plinian eruption and before rapid lava effusion. This is probably related to the extensive degassing of magma in the conduit, which played a role in the transition from explosive to effusive eruptions (Mori and Kato, 2013).

Detailed analytical procedures

Sample polishing

The cut surfaces of samples were polished using alumina powder with a grain size of 1.0 μm. These polished surfaces were further treated by Ar-ion milling (GATAN PIPS Model 691) with an acceleration voltage of 5 kV at an incident angle of 3° for 10 min for FE-SEM observations.

SEM observations

We obtained digital BSE images of the polished sections using a W-SEM (Hitachi High-Technologies S-3400N) at an acceleration voltage of 15 keV and a magnification of ×1000, and with an in-lens type high-resolution FE-SEM (Hitachi High-Technologies S-5500) at acceleration voltages of 10 and 15 keV and a

magnification of $\times 5000$. For higher magnification observations with FE-SEM, we applied lower acceleration voltages (2 keV).

EPMA analyses

We analyzed the chemical compositions of the crystals by energy dispersive spectroscopy (EDS) using electron probe microanalyzers (Oxford INCA-Xact and Thermo Scientific NORAN System7 (NSS) attached to the W-SEM and FE-SEM, respectively). The W-SEM-EDS analysis was performed at an acceleration voltage of 15 keV and a beam current of 1 nA using an X-ray pump probe X-ray intensity reduction routine. The bulk groundmass compositions were determined by area scanning to minimize the loss of Na. The FE-SEM-EDS analysis was performed at acceleration voltages of 15 and 20 kV and beam currents of 0.1–0.7 nA using the PROZA (Phi-Rho-Z) matrix correction algorithm. X-ray maps were analyzed using COMPASS, which is the optional software module of NSS312, to identify mineral phases, measure area fractions, and conduct semi-quantitative FE-SEM analyses of solid solution compositions of the small crystals (size: ca. 1–6 μm) at high magnifications. We conducted the multiple classification analysis of the original EDS spectral imaging data and extracted each principal component spectrum to image peak maps that separate overlapping X-ray intensities at phase boundaries. Mineral compositions were screened on the basis of stoichiometry and total weight proportions.

Water content analyses and fragmentation depth calculations

We analyzed the bulk rock water contents of the samples by conducting manometric analyses using an evacuated glass line. The samples were ultrasonically rinsed with deionized distilled water for 1.5 h in total by changing the water every 15 min; thereafter, the samples were dried in an oven at 110°C. The dried samples were crushed into fine powders using a tungsten carbide mortar. Approximately 1 g of rock samples was used for each analysis. Because each sub-Plinian pumice clast weighs ca. 0.3 g, 10 pumice clasts were crushed and mixed into a homogeneous powder, which was analyzed in triplicate. Two pieces of dense juvenile fragments were crushed and mixed, and then analyzed in triplicate. The vulcanian pumice clasts were large enough for manometric analyses; hence, three pumice clasts were analyzed separately.

Approximately 1.0 g of the powder was heated in a silica glass tube kept under vacuum at 110°C for 30 min and then at 120°C for 30 min to remove the water adsorbed on the surface. Next, the sample was heated to 500°C in approximately 10 min and was kept for 0.5–1 h until the degassing flux decreased. The extracted volatiles were oxidized in a CuO furnace at 460°C and trapped using liquid nitrogen; during this process, the magmatic water that had degassed as a form of hydrogen was transformed into water. The sample temperature was then increased to 1100°C in steps of 200°C in ca. 5 h and was kept for 0.5–1 h to ensure that almost all the volatiles were removed from the sample. The trapped water was purified by changing the refrigerant from liquid nitrogen to a mixture of CO₂(s) (dry ice) and ethanol, and then was cryogenically introduced to a Pyrex flask whose volume was calibrated beforehand. The pressure of the gas was then measured using a ceramic capacitance manometer (Ulvac, Inc. CCMT-100D), and the mass of water was calculated using the equation of state of an ideal gas. The accuracy of the water content obtained in these processes was typically less than 100 ppm.

The water contents of the interstitial glasses were calculated from the bulk rock water contents and modal compositions of the crystals (Table DR1) assuming that the microlites did not contain water. The saturation pressure corresponding to the water contents was then calculated at the assumed temperature of 900 °C (Suzuki et al., 2013), according to the solubility model of Liu et al. (2005). The fragmentation depths were then calculated by assuming that the densities of the overlying magma (for the sub-Plinian stage) and rocks (for the vulcanian stage) in the conduit were 1.3×10^3 and 2.5×10^3 kg/m³, respectively. Here, the vesicularity of the conduit magma was assumed to be similar to that of the sub-Plinian pumices (ca. 53%).

Crystal morphology and CSD stereology

The nanolites and small microlites of low-Ca pyroxene are generally acicular, and often exhibit swallowtail, hopper and hexagonal shapes in the polished sections. Hollow crystals are also common. These morphological characteristics indicate that the crystals grew rapidly under large undercooling. Plagioclase nanolites are generally tabular or acicular, though swallowtail and hopper shapes are also common. The latter

two shapes are rarely observed in plagioclase microlites (Fig. 1). The Fe-Ti oxide microlites with sides longer than 1 μm generally exhibit an euhedral rectangular shape.

To determine the CSDs and area fractions of groundmass crystals on a bubble-free basis, we manually traced the outline of each crystal on the BSE images; the areas and widths were then measured using ImageJ software. The total analyzed areas for sub-Plinian pumices, vulcanian pumices, and vulcanian dense juvenile fragments were 170573, 153363, and 63586 μm^2 , respectively, using the W-SEM and 26613, 8220, and 5315 μm^2 , respectively, using the FE-SEM.

The two-dimensional (2D) measurement of CSD in a cut-section is associated with two primary problems (Peterson, 1996; Higgins, 2000): (1) the intersection probability effect (Royet, 1991), and (2) cut-section effects. The latter includes modification of crystal shape and the effects of fabrics (e.g., foliation or lineation). In order to correct these artifacts, various recalculation methods have been proposed to convert 2D data to 3D. In particular, a combination of the algorithms of *CSDslice* (Morgan and Jerram, 2006) and *CSDCorrections* (Higgins, 2000) has been adopted widely in recent studies. In the present study, however, we did not adopt these corrections owing to the reasons described in the text. Therefore, when comparing the values in the CSDs of the present study to other published CSDs corrected with the above methods, it should be noted that, when the prismatic crystals (whether in width or in length) or the tabular crystals (in width) are measured, the range of crystal size in CSD plots is greater in the corrected data, by a magnitude that corresponding to a factor of the aspect ratio. It is also noteworthy that the y-intersects ($\text{Ln}N_0$) for the width and length of crystals with large aspect ratios are different even for the same sample irrespective of the stereological correction methods.

REFERENCES

Geospatial Information Authority of Japan (GSI), GSI Maps:

<http://geolib.gsi.go.jp/node/2375> (April 2014).

Higgins, M.D., 2000, Measurement of crystal size distributions: The American Mineralogist, v. 85, p. 1105–1116.

Japan Coast Guard (JCG) Hydrographic and Oceanographic Department, 2013:

<http://www1.kaiho.mlit.go.jp/jishin/sokuryo/sokuryo.html> (April 2014).

Japan Meteorological Agency (JMA), 2013, National Catalogue of the Active Volcanoes in Japan (The Fourth Edition, English Version):

http://www.data.jma.go.jp/svd/vois/data/tokyo/STOCK/souran_eng/menu.htm
(April 2014).

Kamada, T., MapMap ver.6.0, A blank map:

<http://www5b.biglobe.ne.jp/t-kamada/CBuilder/mapmap.htm> (April, 2014).

Kozono, T., Ueda, H., Ozawa, T., Koyaguchi, T., Fujita, E., Tomiya, A., and Suzuki, Y.J., 2013, Magma discharge variations during the 2011 eruptions of Shinmoe-dake volcano, Japan, revealed by geodetic and satellite observations: *Bulletin of Volcanology*, v. 75, doi:10.1007/s00445-013-0695-4.

Liu, Y., Zhang, Y., and Behrens, H., 2005, Solubility of H₂O in rhyolitic melts at low pressures and a new empirical model for mixed H₂O–CO₂ solubility in rhyolitic melts: *Journal of Volcanology and Geothermal Research*, v. 143, p. 219–235, doi:10.1016/j.jvolgeores.2004.09.019.

Morgan, D.J., and Jerram, D.A., 2006, On estimating crystal shape for crystal size distribution analysis: *Journal of Volcanology and Geothermal Research*, v. 154, p. 1–7, doi:10.1016/j.jvolgeores.2005.09.016.

Mori, T., and Kato, K., 2013, Sulfur dioxide emissions during the 2011 eruption of Shinmoedake volcano, Japan: *Earth Planets Space*, v. 65, p. 573–580, doi: 10.5047/eps.2013.03.04.005.

Nagahama, H., Saito, H., and Oka, S., 1987, How to Express the symbol diagram of north (True, Magnetic and Grid North) on Maps: *Japan Society of Engineering Geology*, v. 28(1), p.25–34, doi: 10.5110/jjseq.28.25.

Nakada, S., Nagai, M., Kaneko, T., Suzuki, Y., and Maeno, F., 2013, The outline of the 2011 eruption at Shinmoe-dake (Kirishima), Japan: *Earth Planets Space*, v. 65, p.475–488, doi: 10.5047/eps.2013.03.016.

Peterson, T.D., 1996, A refined technique for measuring crystal size distributions in thin section: *Contribution to Mineralogy and Petrology*, v. 124, p. 395–405.

Royet, J.-P., 1991, Stereology: A method for analyzing images: *Progress in Neurobiology*, v. 37, p. 433–474, doi:10.1016/0301-0082(91)90009-P.

Sato, H., Suzuki-Kamata, K., Sato, E., Sano, K., Wada, K., and Imura, R., 2013, Viscosity of andesitic lava and its implications for possible drain-back processes in the 2011 eruption of the Shinmoedake volcano, Japan: *Earth Planets Space*, v. 65, p. 623–631, doi: 10.5047/eps.2013.05.018.

Ueda, H., Kozono, T., Fujita, E., Kohno, Y., Nagai, M., Miyagi, Y., and Tanada, T., 2013, Crustal deformation associated with the 2011 Shinmoe-dake eruption as observed by tiltmeters and GPS: *Earth Planets Space*, v. 65, p. 517–525, doi: 10.5047/eps.2013.03.001.

TABLE DR1 BULK AND GLASS COMPOSITIONS

Modal / chemical compositions	Sub-Plinian pumice	Vulcanian pumice	Dense juvenile fragment
Phenocryst (area %)*		32	29.5
Microlite (area %) ^{†, §}	[5]	[5]	[3]
Plagioclase	20.3	14.8	17.4
Pyroxene	7.9	2.5	4.3
Nanolite (area %) ^{†, §}	[6]	[5]	[3]
Plagioclase	-	11.2	6.7
Pyroxene	5.5	6.3	5.9
Bulk H ₂ O (wt.) ^{†, #}	[3]	[3]	[2]
	0.16 (0.04)	0.22 (0.06)	0.21 (0.03)
Bulk Groundmass (wt.) ^{§§, ##}	[9(5)]	[8(4)]	[6(2)]
SiO ₂	63.03 (0.74)	63.47 (0.87)	63.45 (0.84)
TiO ₂	0.76 (0.06)	0.69 (0.11)	0.73 (0.05)
Al ₂ O ₃	16.81 (0.70)	17.00 (1.22)	16.75 (1.21)
FeO ^{***}	5.88 (0.39)	5.23 (1.10)	5.64 (0.75)
MgO	2.03 (0.18)	2.02 (0.94)	2.09 (0.47)
CaO	5.79 (0.41)	5.79 (0.30)	5.62 (0.48)
Na ₂ O	3.48 (0.07)	3.45 (0.16)	3.38 (0.14)
K ₂ O	2.22 (0.15)	2.37 (0.10)	2.36 (0.16)
Total ^{††}	100	100	100
Matrix H ₂ O (wt.) (including nanolites) ^{***}	0.33 (0.08)	0.39 (0.10)	0.39 (0.05)
Glass H ₂ O (wt.) ^{***}	0.35 (0.08)	0.47 (0.12)	0.44 (0.06)

*Sato et al. (2013).

[†]Numbers in square brackets represent the number of BSE images analyzed for modal compositions, and for number of samples for H₂O content.

[§]Note that the microlites and nanolites were distinguished on the basis of kinks in the CSD slope. Plagioclase microlites actually include nanometer scale crystals, and the nanolites include some crystals with widths up to 1.6–2.6 μm .

[#]Standard deviations are shown in the parentheses.

^{**}Total iron as FeO.

^{††}Recalculated to 100%.

^{§§}Compositions containing microlites and nanolites.

^{##}Numbers in square brackets represent the number of the analyzed area, with the number of analyzed grains in the parentheses.

^{***}Recalculated from the bulk H₂O content and bulk crystallinity (i.e., modal composition of phenocrysts and microlites) using the following density (g/cm³): 3.8 (olivine), 3.4 (pyroxene), 2.7 (plagioclase), 5.2 (Fe-Ti oxide), and 2.35 (bulk groundmass including glass, microlites and nanolites).

TABLE DR2 POPULATION DENSITY (cm⁻⁴)

Size ranges and crystal types	Sub-Plinian pumice	Vulcanian pumice	Dense juvenile fragment
2.6–4.0 µm			
Plagioclase microlites	1.6×10 ¹³	1.6×10 ¹³	1.5×10 ¹³
Pyroxene microlites	7.6×10 ¹²	4.9×10 ¹²	4.8×10 ¹²
0.5–1.6 µm			
Plagioclase nanolites and microlites [*]	3.0×10 ¹⁴	1.4×10 ¹⁵	1.4×10 ¹⁵
Pyroxene nanolites	4.7×10 ¹⁵	3.8×10 ¹⁵	5.6×10 ¹⁵

^{*}Plagioclase crystals in this size range are microlites for the sub-Plinian pumices, while nanolites in the vulcanian pumices and dense juvenile fragments.

TABLE DR3 COMPOSITIONS OF PLAGIOCLASE AND LOW-Ca PYROXENE

		Plagioclase			Low-Ca Pyroxene						
	Sample	Size range	An [†]	No. counted [§]	Sample	Size range	Wo [†]	En [†]	Fs [†]	Mg# [†]	No. counted [§]
		(μm)	(mol %)			(μm)	(mol %)	(mol %)	(mol %)	(mol %)	
Sub-Plinian pumices	Fine microlite	0.5–3.0	64.74 (7.16)	[50(5)]	Nanolite	0.5–1.6	15.70 (5.62)	41.79 (5.78)	42.51 (5.56)	49.82 (5.82)	[53(5)]
	Course microlite	3.0–6.0	70.44 (3.74)	[5(5)]	Microlite	1.6–6.0	14.96 (7.88)	43.22 (6.20)	41.82 (6.04)	50.82 (5.41)	[30(5)]
Vulcanian pumices	Nanolite	0.5–2.6	51.06 (7.66)	[37(5)]	Nanolite	0.5–1.9	13.00 (3.76)	47.70 (4.44)	39.30 (4.94)	54.87 (5.13)	[32(5)]
	Microlite	2.6–6.0	63.31 (8.66)	[16(5)]	Microlite	1.9–6.0	17.80 (7.01)	44.44 (7.37)	37.76 (4.81)	53.86 (2.51)	[22(5)]
Dense fragments	Nanolite	0.5–2.0	58.51 (7.18)	[21(3)]	Nanolite	0.5–1.9	15.28 (4.17)	43.01 (5.68)	41.71 (5.47)	50.76 (6.05)	[27(3)]
	Microlite	2.0–6.0	64.00 (5.86)	[12(3)]	Microlite	1.9–6.0	11.77 (5.71)	48.25 (5.56)	39.98 (3.96)	54.60 (4.56)	[8(3)]

[†]Standard deviations are shown in the parentheses.

[†]An=Ca/(Ca+Na)_{molar}. Wo=Ca/(Ca+Mg+Fe²⁺)_{molar}, En=Mg/(Ca+Mg+Fe²⁺)_{molar}, Fs=Fe²⁺/(Ca+Mg+Fe²⁺)_{molar}, Mg#=Mg/(Mg+Fe²⁺)_{molar}.

[§]Numbers in square brackets represent the number of the analyzed crystals, with the number of analyzed grains in the parentheses.

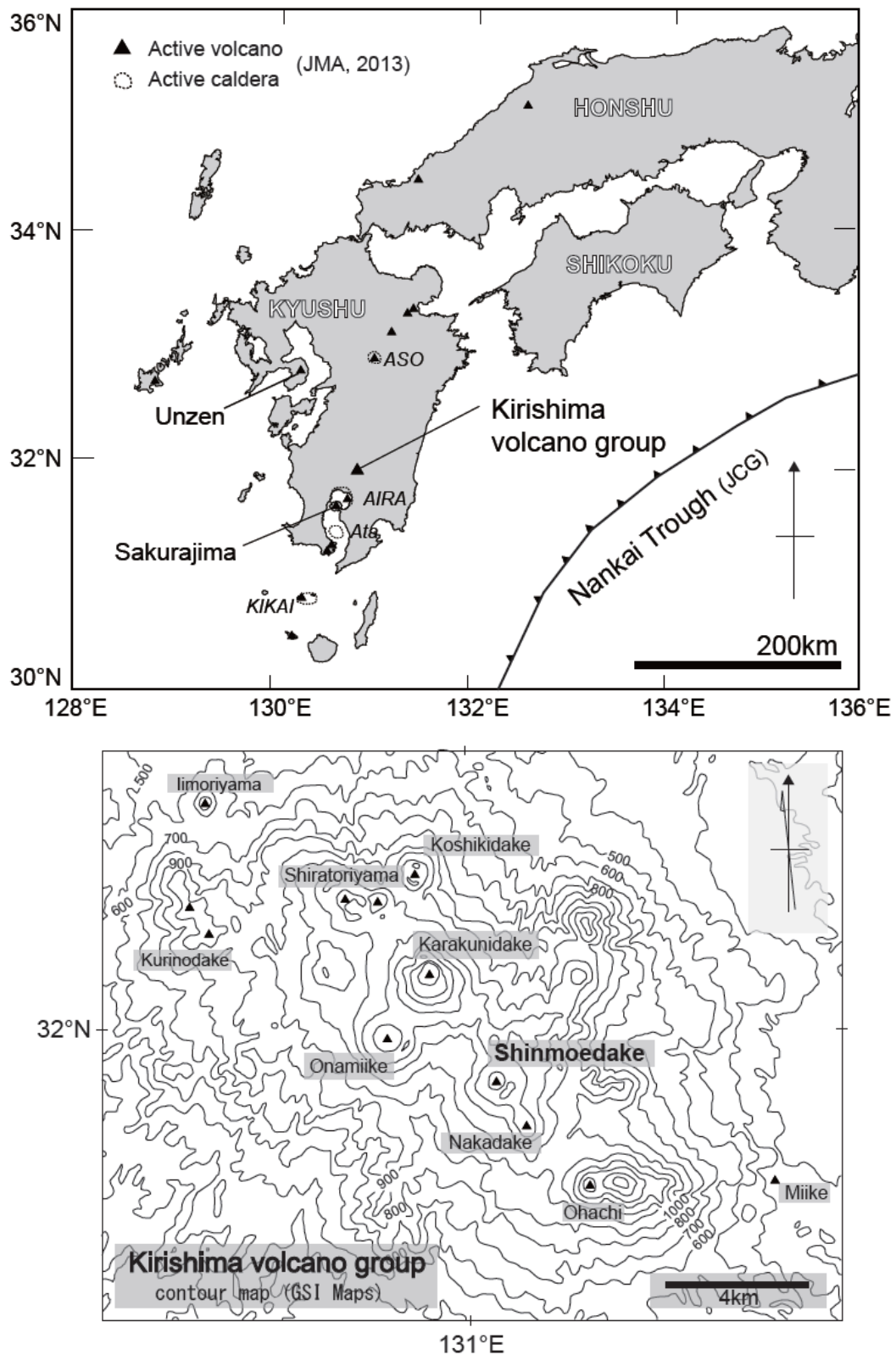


Figure DR1. Location and contour map of Kirishima volcano group. The blank map and contour map were based on MapMap (ver.6.0) and GSI Maps, respectively. The data regarding active volcanoes and calderas, and the Nankai trough were obtained from the Japan Meteorological Agency (JMA, 2013) and Japan Coast Guard (JCG, 2013), respectively.

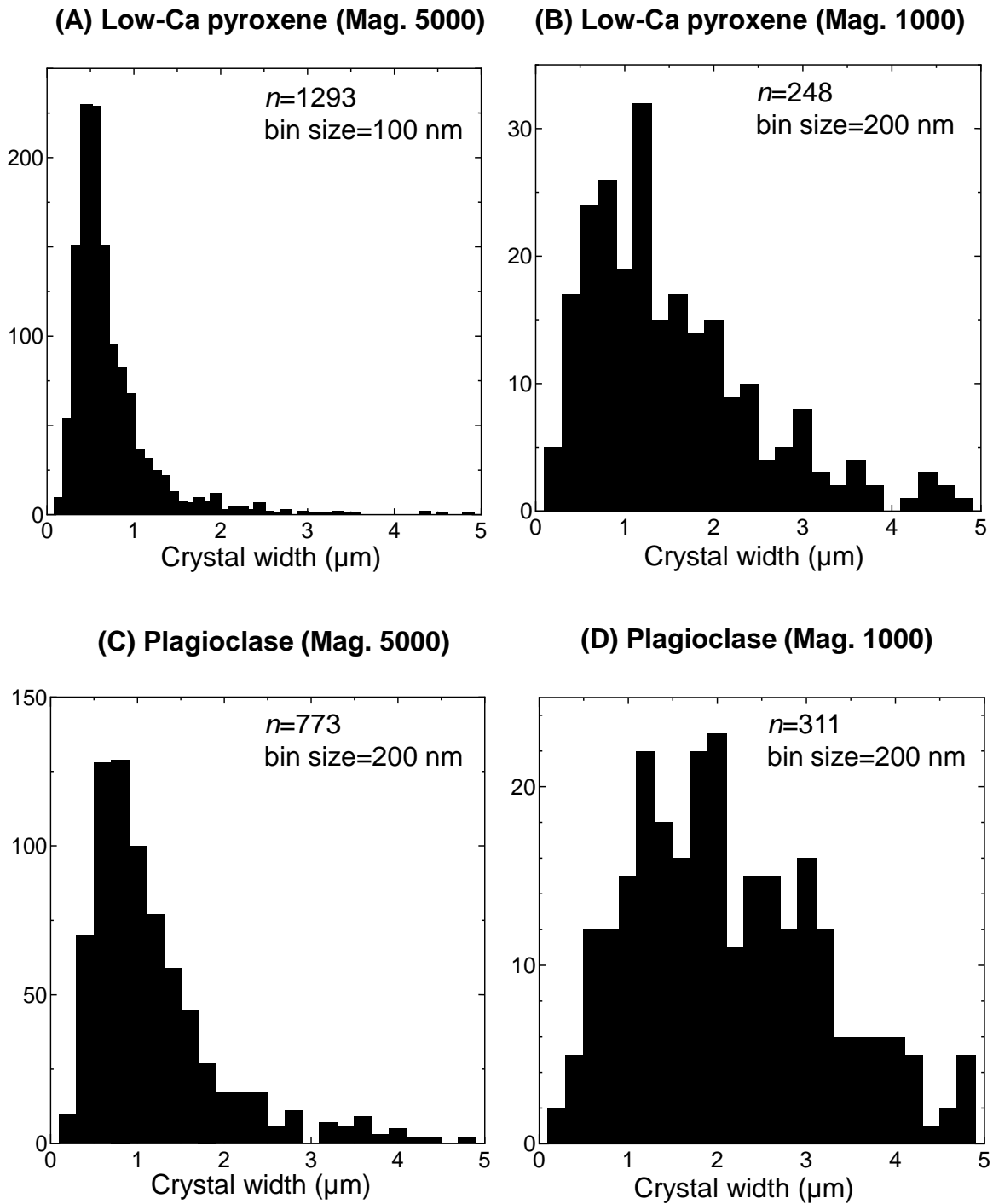


Figure DR2. Crystal width frequency histograms for sub-Plinian pumices obtained from back-scattered electron (BSE) images taken with a field emission scanning electron microscope (FE-SEM) at a magnification of $\times 5000$ (A, C) and with an SEM with a tungsten filament (W-SEM) at a magnification of $\times 1000$ (B, D).